

# Visualizing highly selective electrochemical CO<sub>2</sub> reduction on a molecularly dispersed catalyst



K. Li <sup>a,1</sup>, W. Wang <sup>a,1</sup>, H. Zheng <sup>b,1</sup>, X. Wang <sup>b</sup>, Z. Xie <sup>a</sup>, L. Ding <sup>a</sup>, S. Yu <sup>a</sup>, Y. Yao <sup>b,\*\*</sup>, F.-Y. Zhang <sup>a,\*</sup>

<sup>a</sup> Nanodynamics and High-Efficiency Lab for Propulsion and Power, Department of Mechanical, Aerospace & Biomedical Engineering, UT Space Institute, University of Tennessee, Knoxville, Tullahoma, TN, 37388, USA

<sup>b</sup> Department of Electrical and Computer Engineering and Texas Center for Superconductivity at the University of Houston (TcSUH), University of Houston, Houston, TX, 77204, USA

## ARTICLE INFO

### Article history:

Received 24 February 2021

Received in revised form

18 April 2021

Accepted 26 April 2021

Available online 4 May 2021

### Keywords:

Electrochemical CO<sub>2</sub> reduction

CO synthesis

Molecularly dispersed electrocatalyst

Optical visualization

High-speed and micro-scale visualization system

Bubble behaviors

## ABSTRACT

Electrochemical CO<sub>2</sub> reduction driven by renewable electricity provides a promising strategy for the ambient synthesis of CO. While great efforts were being devoted to developing highly efficient catalysts for electrochemical CO<sub>2</sub> reduction reactions (CO<sub>2</sub>RRs), electrode improvement is another important direction for the real-world application of CO<sub>2</sub> conversion. Toward a better understanding on the mechanism of the highly selective CO<sub>2</sub>RR catalyst on the electrode, an *in-situ*, high-resolution, and high-speed microscale visualization techniques are applied to observe the generation and detachment of the CO<sub>2</sub>RR products (CO and H<sub>2</sub>) on the electrode coated with molecularly dispersed electrocatalyst of methoxy group functionalized nickel phthalocyanine (NiPc-OMe MDE). The catalyst exhibits superb selectivity towards CO formation with Faradic efficiency above 98% from  $-0.56$  V to  $-0.77$  V vs. RHE and approaches 100% at  $-0.65$  V vs. RHE. The CO and H<sub>2</sub> bubbles are observed in CO<sub>2</sub> and Ar atmosphere, which provide direct evidence for the high selectivity of NiPc-OMe MDE. Additionally, the number of reaction regions and their gas production rate increase as the applied cathodic potential increases. The *in-situ* optical visualization method employed in the electrochemical test system contributes to better electrode design of the CO<sub>2</sub> electrolyzer to accelerate the transition from lab-scale investigation to industrialization.

© 2021 Elsevier Ltd. All rights reserved.

## 1. Introduction

Excessive carbon dioxide (CO<sub>2</sub>) emissions caused by the consumption of traditional fossil fuels have driven severe global environmental problems [1–4]. The development of eco-friendly and high-efficiency clean energy based on proton electrolyte membrane electrolyzer cells is an urgent and prospective strategy to break out the knotty problem [5–11]. Meanwhile, speeding up the progress in the use of CO<sub>2</sub> is essential for achieving sustainable human activities through carbon recycling [12]. With the convenience and declined price of electricity generated from renewable sources, e.g., biomass, geothermal, solar, tides, hydroelectricity, and wind, electrochemical conversion of CO<sub>2</sub> into fuels and value-added

chemicals is a promising and significant solution to relieve the concentration of CO<sub>2</sub> operated under ambient atmosphere [13–15]. The use of appropriate electrocatalysts could perform the electrochemical CO<sub>2</sub> reduction reaction (CO<sub>2</sub>RR) to generate various products, which include formate [16–18], carbon monoxide (CO) [19–21], formic acid [22], C<sub>1</sub> products (methane and methanol) [23,24], C<sub>2</sub> products (ethylene and ethanol) [25–27], C<sub>3</sub> (*n*-propanol) [28], etc. CO was considered to be one of the most profitable feedstocks among the above potential products due to the advantages of the corresponding reaction requiring only two electrons and two protons bringing up high yield and selectivity, as well as the facilitated separation of gaseous and electrolyte during the electrochemical synthesis process [29]. Additionally, the broad applications of CO in energy, chemical, transportation, metallurgical, and pharmaceutical industries arouse plentiful attention and prospect in large-scale synthesis technology [30]. Nevertheless, developing cost-effective electrocatalysts affording low energy losses and high efficiencies is still a major challenge to permit the

\* Corresponding author.

\*\* Corresponding author.

E-mail addresses: [yyao4@uh.edu](mailto:yyao4@uh.edu) (Y. Yao), [fzhang@utk.edu](mailto:fzhang@utk.edu) (F.-Y. Zhang).

<sup>1</sup> These authors contributed equally to this work.

practical application [31,32]. Thus, the profound and comprehensive understanding of the mechanism and application of electrochemical CO<sub>2</sub> conversion to CO exhibits special importance to design efficacious catalysts [33].

As to the reaction schematic of CO<sub>2</sub>RR in aqueous electrolyte, Hori et al. firstly proposed a rational electrochemical pathway of CO<sub>2</sub> conversion to CO based on the numerous experimental data and electrode reaction dynamics [34–36]. The system deviations of experimental results and many simplifications in the formulaic derivation would limit the depth of the research method. Theoretical calculations on the pathways through various products formation for CO<sub>2</sub>RR employing the density functional theory (DFT) formalism could not only provide a guidance on mechanism study, and also inspire the rational design of novel electrocatalyst [37,38]. However, the related computational models assumed on a single or ideal crystalline surface could not fully reflect the real reaction processes, which was influenced by the microenvironments. With the rise of *in-situ* infrared spectroscopy since the 1970s, this technique has been commonly used to monitor the interaction between molecules of intermediates and products on the catalyst surface in the solution [39–41]. Recent research efforts in the application of *in-situ* infrared spectroscopy have been afforded to understanding the underlying mechanism and kinetics of the CO<sub>2</sub>RR behind the high activity and selectivity by tracking the reaction intermediates in operando conditions [42–44]. Though *in-situ* infrared spectroscopy studies have been conducted in the electrode/electrolyte system, there is a lack of deep understanding of the various influencing factors in a real-world application.

In this work, to investigate how electrocatalytic behaviors including the generation and detachment of product (CO and H<sub>2</sub>) bubbles occur at the electrode surface, the *in-situ* micro-scale visualization technique is first-time employed to directly observe the electrochemical reduction of CO<sub>2</sub> to CO on the significantly efficient electrocatalyst of nickel phthalocyanine with methoxy group functionalization (NiPc-OMe), which is synthesized via molecularly dispersing on multi-walled carbon nanotubes (CNTs). The performance towards CO formation of the as-researched catalyst is investigated by electrochemical measurements, *in-situ* gas chromatograph (GC), and *ex-situ* nuclear magnetic resonance (NMR) analysis over the potential range from –0.56 V to –0.77 V vs. reversible hydrogen electrode (RHE), exhibiting a significantly high Faradic efficiency (FE) and selectivity as well as CO generation rate. The high-resolution and micro-scale visualization helps us directly view CO generation at the electrode in the CO<sub>2</sub>-saturated 0.5 M KHCO<sub>3</sub> electrolyte. Additionally, it is revealed that the behaviors of CO bubbles are influenced by the applied cathodic potential analyzed via high-speed and micro-scale visualization system (HMVS). Moreover, by comparison of the electrode in CO<sub>2</sub>- and Ar-saturated electrode, the visualization results illustrate the high selectivity of NiPc-OMe for CO<sub>2</sub>RR. This method of *in-situ* micro-scale visualization in the electrochemical test system also raises the inspiration in the electrode design and development of the CO<sub>2</sub> electrolyzer to accelerate the process to practical application.

## 2. Experimental section

### 2.1. Catalyst synthesis

The NiPc-OMe was synthesized referring literature with some modifications [45,46]. Specifically, 4-nitrophthalonitrile (4.0 g) was dissolved in a mixed solvent of methanol (10 ml) and dimethylformamide (60 ml). Subsequently, K<sub>2</sub>CO<sub>3</sub> (8.0 g) was added to the solvent under Ar atmosphere, stirring at 70 °C for 3 h. The mixture was diluted with water (150 ml) and dichloromethane (150 ml) to obtain separated layers. Then, the aqueous layer was

extracted with dichloromethane for 3 times. The combined organic layer was dried over MgSO<sub>4</sub>, filtered, and concentrated. The crude 4-methoxyphthalonitrile was purified by silica gel flash column chromatography (elution with dichloromethane), to result in a white powder. Then, 4-methoxyphthalonitrile (2.7 g) and nickel acetate tetrahydrate (1.35 g) were dissolved in 50 ml of sulfonate. After well mixing, 1,8-diazabicyclo[5.4.0]undec-7-ene (0.6 ml) was added and the mixture was stirred at 160 °C for 10 h. After the reaction was completed, methanol was added to precipitate solid products. The collected solid was purified by Soxhlet extraction. Finally, the NiPc-OMe was obtained as a dark green solid.

### 2.2. Preparation of the NiPc-OMe molecularly dispersed electrocatalyst (MDE)

Typically, 30 mg of purified CNTs were dispersed in 20 ml DMF by sonication. Meanwhile, a calculated amount NiPc-OMe (~5 mg) was dissolved in DMF with the assistance of sonication. The sonication procedure is essential to ensure the NiPc-OMe in single molecule dispersion. Subsequently, the above two mixtures were combined together and performed a continual sonication for 1 h. Then the mixture was stirred for another 12 h at room temperature. The solid was collected by centrifuged and washed with DMF, ethanol, and water successively. After that, the obtained powder was then lyophilized drying to yield the final NiPc-OMe MDE product.

### 2.3. Materials characterizations

Scanning electron microscope (SEM) imaging was conducted using Gemini LEO 1525 microscopy. Transmission electron microscope (TEM) and energy dispersive X-ray spectroscopy (EDS) were conducted using FEI Tecnai G2 F30 transmission electron microscope. Inductively coupled plasma mass spectrometry (ICP-MS) was carried out using Agilent Technologies 7700 series instrument. X-ray absorption spectroscopy (XAS) was collected by employing synchrotron radiation light source at Beamline 12-BM of the Advanced Photon Source in Argonne National Laboratory. The Ni K-edge of standard nickel foil was used for energy calibration. Extended X-ray absorption fine structure (EXAFS) spectra were fitted using the Athena and Artemis software packages.

### 2.4. Electrochemical characterizations

All electrochemical measurements were conducted in a three-electrode system controlled by the electrochemical workstation (Squidstat SUI v2.0). Graphite rod and KCl saturated Ag/AgCl electrode were applied as the counter electrode and reference electrode, respectively.

To prepare the catalyst ink, 2.0 mg hybrids were dispersed in 1 ml ethanol solution containing 0.0325 wt% Nafion with sonication for 1 h. The NiPc-OMe ink was obtained in DMF (2.0 mg ml<sup>-1</sup>). Then, 100 μl ink was drop-casted on a carbon fiber paper (Toray, TGH-H-060, 190-μm-thick) in the size of 0.50 cm (width) and 1.0 cm (length) to prepare the working electrode with a loading of 0.40 mg cm<sup>-2</sup>. All electrochemical experiments were carried out at room temperature. 0.5 M CO<sub>2</sub>-saturated KHCO<sub>3</sub> solution (pH = 7.2) was used as the electrolyte solution. All current density in the unit of mA cm<sup>-2</sup> was calculated from the electrode geometric (0.5 cm<sup>2</sup>), and all potentials were converted to versus RHE with *iR* corrections.

### 2.5. In-situ visualization system

A high-speed and micro-scale visualization system (HMVS) was developed to capture the electrochemical reactions on the

electrodes. With the help of Phantom v711 camera and micro-scale lens, the HMVS can capture videos with a resolution of  $1280 \times 800$  under recording fps of 7530. Through HMVS, Mo et al. firstly discovered the real active sites across the entire catalyst layer in water electrolyzer cell in microspatial and microtemporal scales [5]. And then, the team utilized this novel system to *in-situ* investigate the electrochemical oxygen evolution reactions, revealing that the OER reactions only occur on the anode catalyst layer adjacent to the liquid/gas diffusion layer (LGDL) [10]. Further, Li et al. investigated the influence of LGDL wettability on the oxygen bubble dynamics and detachment process [47]. Coupling with the HMVS, a three-electrode system with transparent cells was also developed. In this system, the electrodes were fixed vertically in the electrolyte for observation. High-speed videos for bubble generation, growth, and detachment were recorded at the potential of  $-0.65$  and  $-0.7$  V vs. RHE with *iR* correction.

### 3. Results and discussion

Metal phthalocyanine has been reported as a class of remarkable molecular catalysts for  $\text{CO}_2\text{RR}$  due to the well-defined metal- $\text{N}_4$  catalytical active sites [15]. NiPc-OMe with electron donating substituents was proved to have excellent and robust activity for  $\text{CO}_2\text{RR}$  [20]. Notably, the molecularly dispersed metal phthalocyanine on CNTs exhibits prominent catalytic activity [19]. The NiPc-OMe MDE was constructed through attaching the molecule on CNTs as shown in Fig. 1a inset. Ni content in NiPc-OMe hybrid was  $\sim 0.7$  wt% confirmed by ICP-MS measurement, corresponding 8.2% of NiPc-OMe molecule in the hybrids MDE.

Electron microscopy images from TEM and SEM showed no particle aggregations, indicating that NiPc-OMe molecules were highly dispersed on the surface of CNTs (Fig. 1a and b). And it was clearly observed in Fig. 1b that the structure of CNTs was well maintained with a uniform interwall distance of 0.350 nm. X-ray absorption near-edge structure (XANES) and EXAFS were used to investigate the local atomic and electronic structures of chemical constituents of NiPc-OMe MDE. As shown in Fig. 1c, pre-edge features appear at 8342 eV, assigning to the signature of Ni atoms in

the square-planar metal- $\text{N}_4$  moieties with distorted  $\text{D}_{4h}$  symmetry [48]. The EXAFS spectra (inset of Fig. 1c) showed only a dominant peak at 1.45 Å (Ni–N bond) and the absence of a peak at 2.15 Å (Ni–Ni bond), confirming the Ni atoms are isolated in NiPc-OMe MDE. Furthermore, Fig. 1d revealed the homogenous distribution of C, N, and Ni elements over the entire NiPc-OMe MDE.

The activity of the NiPc-OMe MDE was evaluated in  $\text{CO}_2$ -saturated 0.5 M  $\text{KHCO}_3$  in a two-compartment electrochemical cell. Notably, benefiting from the well-dispersed Ni–N active sites and superb conductivity of hybrids, NiPc-OMe MDE could show outstanding catalytic properties. As shown in Fig. 2a, the current density of NiPc-OMe MDE was up to  $34.6 \text{ mA cm}^{-2}$  at  $-0.73$  V, which was significantly higher than those of pure CNTs, suggesting the true catalytic performance comes from NiPc-OMe molecules. Additionally, the current density at  $-0.73$  V of NiPc-OMe MDE under  $\text{CO}_2$  atmosphere was 23 times higher than that under Ar atmosphere, and the corresponding applied voltage shifted from  $-0.65$  V to  $-0.52$  V at  $1 \text{ mA cm}^{-2}$ . It was certified that the additional increase in current density is attributed to the occurrence of electrochemical reduction of  $\text{CO}_2$ . Besides, it was noted that the as-prepared NiPc-OMe MDE exhibited extremely poor performance to hydrogen evolution reaction (HER) at a large range from  $-0.5$  V to  $-0.77$  V, where the catalyst showed excellent activity for  $\text{CO}_2\text{RR}$ , demonstrating the high selectivity of the NiPc-OMe MDE for  $\text{CO}_2\text{RR}$  instead of the competing reaction.

To analyze the electroreduction products, chronoamperometry (CA) measurements (Fig. 2b) were performed at several potentials for 1 h in  $\text{CO}_2$ -saturated 0.5 M  $\text{KHCO}_3$  aqueous solution. The gas and liquid products were quantified by GC and NMR spectroscopy, respectively. As shown in Figure S1, the results from NMR showed that the main reduction products are CO and  $\text{H}_2$  across a broad voltage range and no liquid reduction product was detected. Notably, the NiPc-OMe MDE was highly selective towards CO formation with FE above 98% from  $-0.56$  V to  $-0.77$  V (Fig. 2c). Especially at  $-0.65$  V, the maximum FE(CO) was approaching 100%. Additionally, the CO partial current density was  $32 \text{ mA cm}^{-2}$  at  $-0.78$  V (Fig. 2c), significantly higher than most reported nickel-based catalysts as compared in Table S1. Moreover, long-term

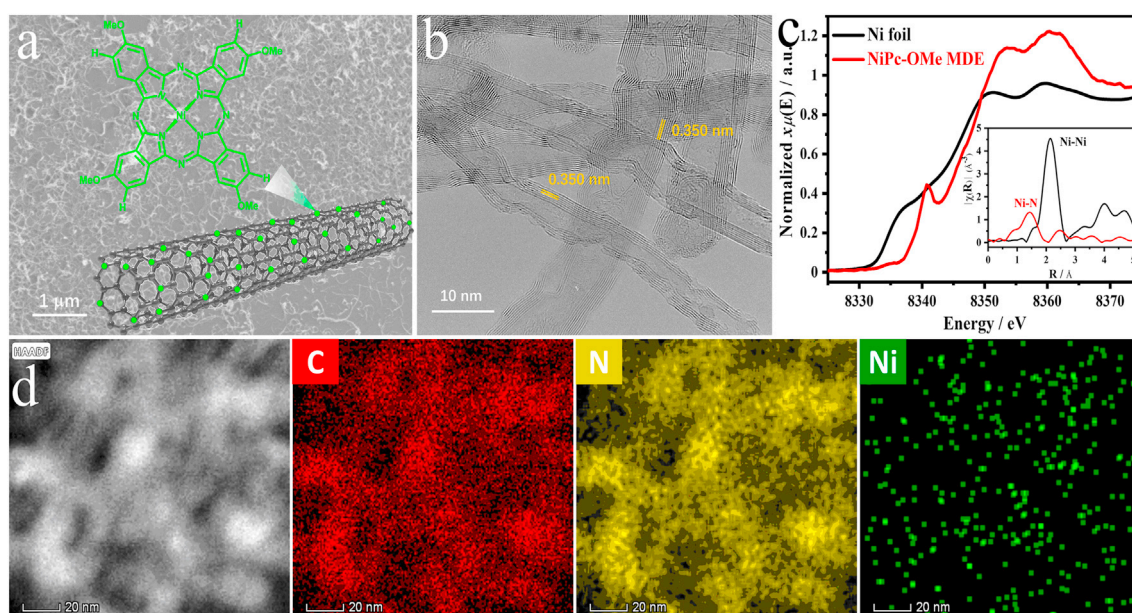


**Fig. 1.** SEM (a) and high-resolution TEM (b) images of NiPc-OMe MDE; The inset shows a schematic illustration of the NiPc-OMe MDEs anchored on the CNTs. (c) Ni K-edge XANES spectra (inset displays Fourier transform of the EXAFS spectra); (d) EDS element mapping of NiPc-OMe MDE.

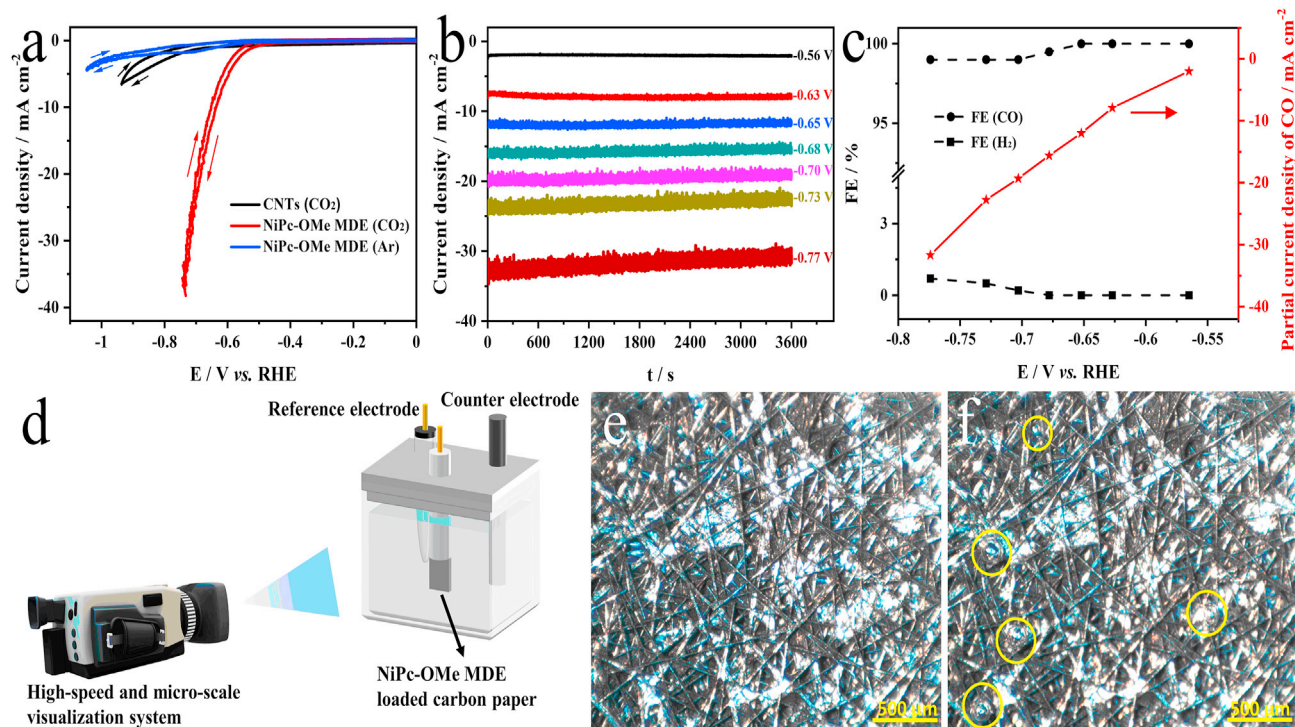


**Fig. 2.** (a) Cyclic voltammograms recorded in  $\text{CO}_2$ - and Ar-saturated 0.5 M  $\text{KHCO}_3$  electrolytes at a scan rate of  $20 \text{ mV s}^{-1}$ . (b) CA curves of NiPc-OMe MDE for 1 h at various potentials in  $\text{CO}_2$ -saturated 0.5 M  $\text{KHCO}_3$  aqueous solution. (c) FE of CO and  $\text{H}_2$  and partial current density of CO at different applied potentials on NiPc-OMe MDE under  $\text{CO}_2$  atmosphere. (d) Schematic of the *in-situ* optical visualization system incorporating with electrochemical test system; The snapshotted images from Supplementary material Movie S1 recorded on the electrode in Ar- (e) and  $\text{CO}_2$ - (f) saturated electrolytes with a controlled potential of  $-0.65 \text{ V}$ .

durability is an important merit for electrocatalyst evaluation. We conducted the durability test by controlling the current density at  $10 \text{ mA cm}^{-2}$  on NiPc-OMe MDE as shown in Figure S2. It was indicated that NiPc-OMe MDE showed outstanding stability for  $\text{CO}_2\text{RR}$  according to the constant potential and non-degradation FE for 20 h. Therefore, the NiPc-OMe MDE is an excellent electrocatalyst for the reduction of  $\text{CO}_2$  to CO with extraordinary activity, high selectivity, and stability.

Blank sample prepared by dropping neat CNTs on the carbon paper was applied under  $\text{CO}_2$  atmosphere at different applied potentials. As shown in the Figure S3, the electrode of CNTs/CP exhibited approximately 100% of FE for  $\text{H}_2$  generation at the potential range from  $-0.5$  to  $-0.68 \text{ V}$ , demonstrating the high FE(CO) of NiPc-OMe MDE/CP was entirely attributed to the molecularly dispersed NiPc-OMe rather than CNTs and carbon paper. In order to further clarify the mechanism of NiPc-OMe MDE enhancing the  $\text{CO}_2\text{RR}$  performance, the electrode prepared by directly dropping NiPc-OMe without CNTs on carbon paper was tested. As shown in the Figure S4a-b, the electrode of NiPc-OMe/CP exhibited the lower current density than the one of NiPc-OMe MDE/CP under the same conditions. The significant FE decrease and poor selectivity of NiPc-OMe/CP without CNTs in Figure S4c indicated that CNTs could not only facilitate the highly uniform dispersion of NiPc-OMe to expose the active sites, but also prevent the molecule aggregation due to  $\pi$ - $\pi$  interaction to low the resistance of the charge transfer from the electrode to the catalyst, thereby improving the catalytic activity and selectivity. Additionally, as explained in the literature based on theoretical calculations, the energy of  $^*\text{H}$  intermediate formation for HER is larger than the one of  $^*\text{COOH}$  intermediate for  $\text{CO}_2\text{RR}$  on the NiPc-OMe [20]. Thus, the NiPc-OMe MDE is more prone to  $\text{CO}_2\text{RR}$  and exhibits high selectivity. And NiPc-based molecular catalysts have appropriate  $\text{CO}_2$  molecular adsorption energy and CO

molecular desorption energy, benefiting to improving FE of CO [49–51].

To further certify the results concluded from the electrochemical test, an *in-situ* micro visualization system with the micrometer resolution was applied to investigate the bubble generation in the electrolyte under ambient conditions. The schematic of the *in-situ* visualization system, which consisted of a high-speed and micro-scale visualization camera and three-electrode electrochemical test system, was illustrated in Fig. 2d. As shown in Fig. 2e, the electrode was vertically soaked in Ar-saturated 0.5 M  $\text{KHCO}_3$  at the potential of  $-0.65 \text{ V}$  and no bubble was detected. Once replacing Ar with  $\text{CO}_2$  as the purging gas, large amounts of bubbles were observed on the electrode surface (Fig. 2f). Combined with the above analysis of GC and NMR for the products, it could be confirmed that the bubbles in Fig. 2f were indeed CO, which was the main product at the  $-0.65 \text{ V}$  in 0.5 M  $\text{KHCO}_3$  for  $\text{CO}_2\text{RR}$ . The obvious difference on the electrode under different gas atmospheres for bubble generation indicated that the NiPc-OMe MDE exhibits high selectivity for electrochemical conversion of  $\text{CO}_2$  to CO. The NiPc-OMe MDE also presents an extraordinary inactivity for HER at the cathodic potential in 0.5 M  $\text{KHCO}_3$  electrolyte, the phenomenon of which is consistent with the comparison results from LSV in Fig. 2a. Additionally, the high-resolution video provided in Movie S1 showed that the CO bubbles continuously generated, detached and moved on the electrode surface at a high frequency.

Supplementary data related to this article can be found at <https://doi.org/10.1016/j.mtphys.2021.100427>.

To acquire detailed information in the extremely rapid electrochemical reaction, we used a high-speed camera to capture the bubble behaviors in the electrochemical  $\text{CO}_2$  reduction process. The CO bubble generation and detachment locations at the potential

of  $-0.65$  V, which were defined as the reaction regions different from reaction sites in nanoscale for electrocatalysis, were shown in Fig. 3a–d. The bubble was marked in a yellow circle. The gas bubbles nucleated at certain locations in the carbon paper (CP), and then held on the electrode surface by strong surface tension, until they grew into a larger size that was able to detach. Once the bubble grew into a sufficient size, it detached and moved along the electrode surface. Initially (Fig. 3a), there was no bubble in the yellow circles. At  $t_0$ , the bubble appeared at the site in the yellow circle, then grew with the reaction progressing. The bubble began to detach from the CP at  $t_0 + 0.277$  s (Fig. 3b). Finally, the bubble moved along the direction noted by the yellow arrow under the dominance of the buoyancy force. For the second bubble, a similar detachment process was also captured as shown in Fig. 3c and d. The detachment time of the second bubble was around  $0.288$  s, which was similar to the first one. The bubbles moved in the same direction as shown in Fig. 3b and d. The bubble transport and detachment processes at the same location and different times are similar. These visual experiment results clarify that the behaviors of the bubble growth, detachment, and transport occurred as regular periodic events, which means the reaction rate is relatively stable. Moreover, the locations of reaction regions are fixed, indicating that the reaction regions do not change with the going of reaction.

Combined with the impact of applied potential on current density as presented in Fig. 2b, the HMVS was performed to capture the bubble behavior under another potential of  $-0.7$  V to facilitate the understanding of the potential influence for  $\text{CO}_2\text{RR}$  in a micro-scale. The sequence of bubble generation was shown in Fig. 3e–h. The location was selected in yellow circle under the same micro-environment with the one tested at  $-0.65$  V to eliminate the influence from the system. The detachment time for the first and second bubbles was very close,  $0.262$  s and  $0.264$  s, respectively, which were shorter than the ones tested at  $-0.65$  V. Additionally, it was noted that the interval between the first and second detachments in Fig. 3f and h was  $0.653$  s, which was shorter than the one ( $0.891$  s) tested at  $-0.65$  V. The visualization results showed that the higher overpotential induced the larger detachment frequency of bubbles. It can be attributed to the higher current density at more negative potential (Fig. 2b), which accelerates the reaction rate. According to the analysis of bubble size from each cycle at the same potential, it was observed a little diameter difference in

between Fig. 3b and d as well as Fig. 3f and h, indicating the stable bubble generation.

As shown in Fig. 4a–f, the bubble sizes were measured to further analyze the effect of electrolysis potential. Specifically, we choose three reaction regions and compared their bubble size at different applied potential. In Fig. 4a–c, the bubble size was  $90.3$   $\mu\text{m}$ ,  $187.6$   $\mu\text{m}$ , and  $243.9$   $\mu\text{m}$ , respectively, which were smaller than the ones of  $96.5$   $\mu\text{m}$ ,  $195.2$   $\mu\text{m}$ , and  $262.6$   $\mu\text{m}$  in Fig. 4d–f, respectively. It was noted that these three locations were in the same microenvironment thus the size increases could be ascribed to the potential change. As statistics the bubble size in Fig. 4g, the bubble size on the electrode was mainly distributed in  $120$ – $200$   $\mu\text{m}$  range. However, at the potential of  $-0.7$  V, partial bubbles' size moves from less than  $120$   $\mu\text{m}$  to the range between  $120$  and  $200$   $\mu\text{m}$  gradually. The average bubble sizes counted from the electrode at the potential of  $-0.65$  V was  $158.8$   $\mu\text{m}$ , which was smaller than the one of  $166.9$   $\mu\text{m}$  at  $-0.7$  V. With the increase of applied cathodic potential from  $-0.65$  to  $-0.7$  V, larger bubbles indicated the higher volume of products. The combination of varied detachment rates and bubble sizes provides a visible evidence for the influence of applied potential on product yield rate, which is consistent with the trend of turnover frequency for CO generation ( $\text{TOF}_{\text{CO}}$ , based on all the molecules loaded on the electrode) in Figure S5. These visualization results provide kinetic information to the catalyst in the process of electrochemical reduction of  $\text{CO}_2$  and CO generation. Moreover, the detachment of bigger bubbles has a larger impact on the reactant/product transport in the reaction regions. As the bubbles covering the reaction regions, the transport of reactant impeded the reaction to some extent. Hence, the periodic detachment could induce the more frequent and severe fluctuation of current density with the applied potential increases as certified in the CA curves in Fig. 2b.

To further explore the origin of electrochemical reduction of  $\text{CO}_2$  on the electrode, the electrochemical reactions under different conditions were captured, as recorded in Movie S4. On one hand, at the electrolysis potential of  $-0.65$  V, Fig. 5a showed that there were only 3 reaction regions observed in an Ar-saturated electrolyte, while there were 12 regions in the  $\text{CO}_2$ -saturated electrolyte in Fig. 5b. The comparisons of the samples conducted in the electrolyte with and without  $\text{CO}_2$  directly indicate additional bubble generation sites were produced. The newly emerged activated

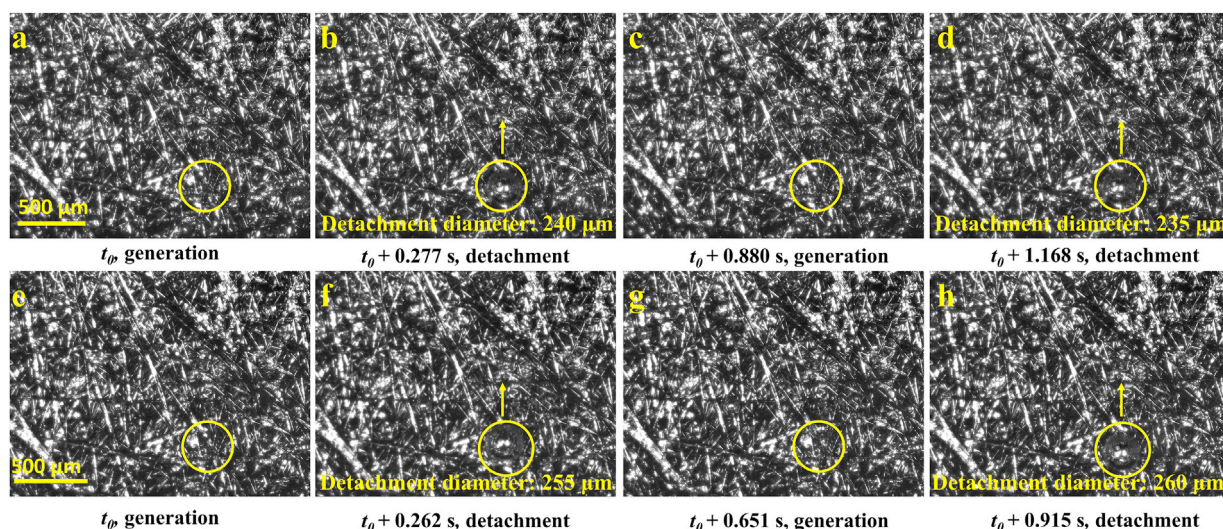
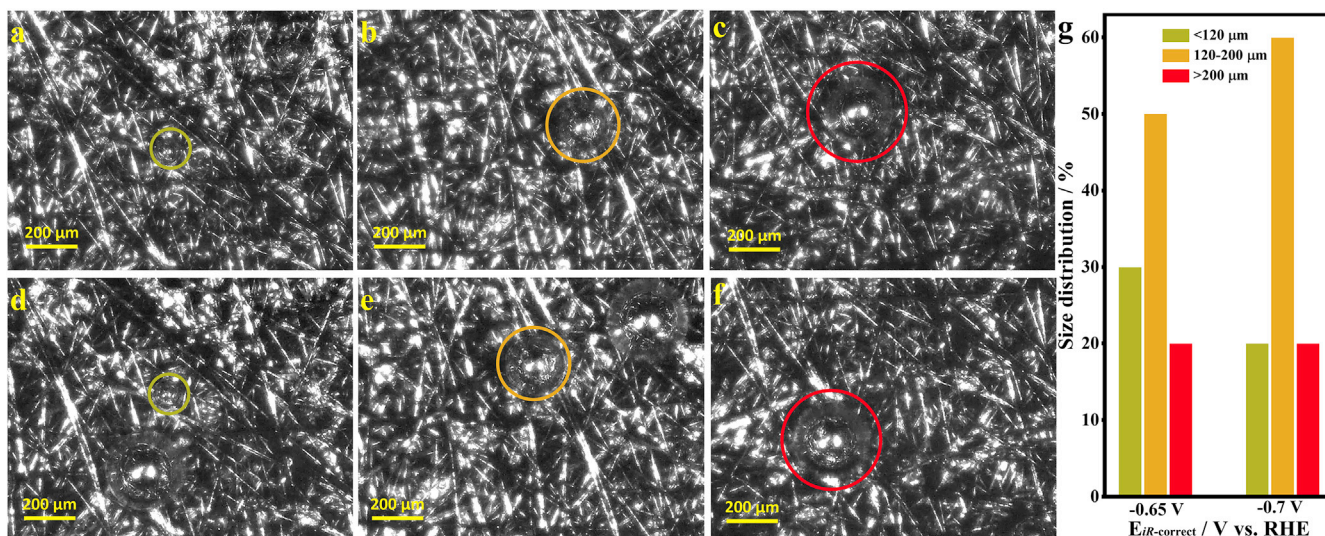
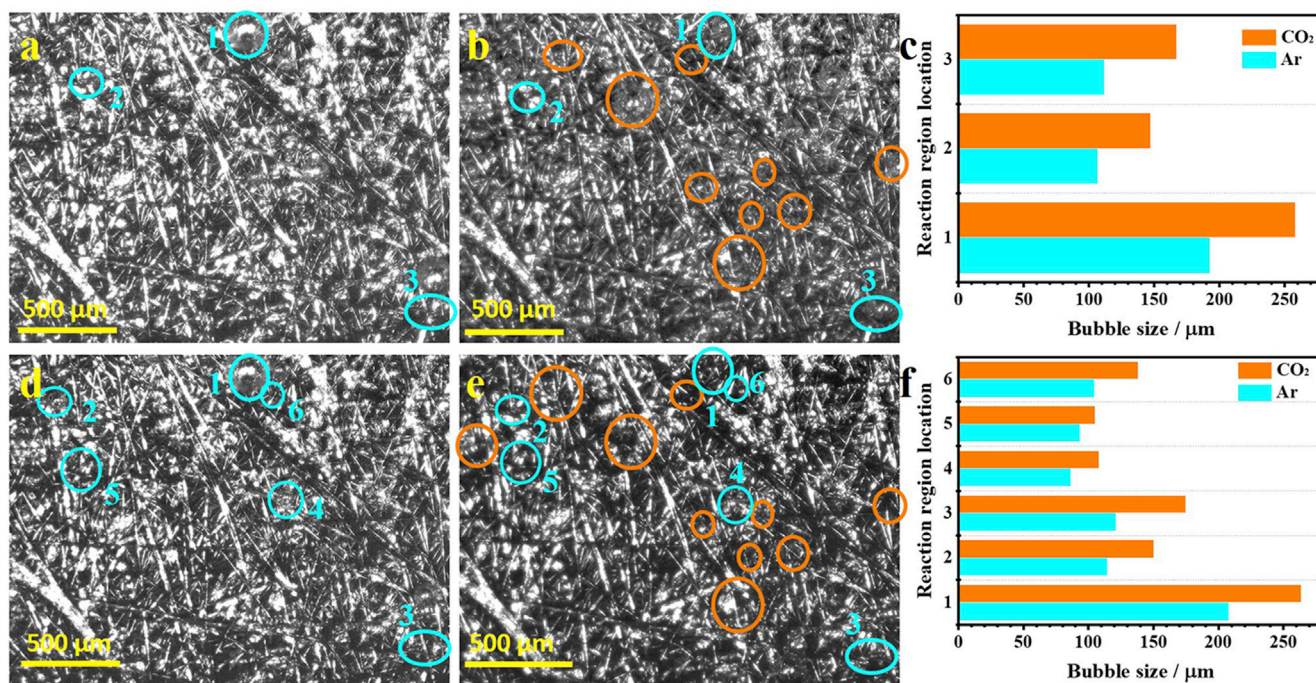


Fig. 3. Sequence of images captured from Movies S2 and S3 recorded via high-speed camera showing the visualization of a single bubble's behaviors in a  $\text{CO}_2$ -saturated electrolyte with a controlled potential of  $-0.65$  V (a–d) and  $-0.7$  V (e–h).



**Fig. 4.** The images captured from Movies S2 and S3: (a–c) At  $-0.65$  V in  $\text{CO}_2$ -saturated  $0.5$  M  $\text{KHCO}_3$ ; (d–f) At  $-0.7$  V in  $\text{CO}_2$ -saturated  $0.5$  M  $\text{KHCO}_3$ ; (g) The statics and summarization of bubble sizes at the electrolysis of  $-0.65$  V and  $-0.7$  V.



**Fig. 5.** Images captured from Movie S4 under difference conditions: (a) At  $-0.65$  V in Ar-saturated  $0.5$  M  $\text{KHCO}_3$ ; (b) At  $-0.65$  V in  $\text{CO}_2$ -saturated  $0.5$  M  $\text{KHCO}_3$ ; (d) At  $-0.7$  V in Ar-saturated  $0.5$  M  $\text{KHCO}_3$ ; (e) At  $-0.7$  V in  $\text{CO}_2$ -saturated  $0.5$  M  $\text{KHCO}_3$ . The comparison of bubble sizes generated between the Ar- and  $\text{CO}_2$ - saturated  $0.5$  M  $\text{KHCO}_3$  at the electrolysis of  $-0.65$  V (c) and  $-0.7$  V (f). All tests operated under ambient atmosphere and corresponding CA curves plotted in Figure S10.

regions marked in orange cycles were ascribed to electrocatalyze  $\text{CO}_2$  reduction. To investigate the effect of gas atmosphere changes on the products, the sizes of bubbles detached from the reaction regions (marked in aqua cycles), where bubbles generated under both Ar and  $\text{CO}_2$  atmospheres, were compared in Fig. 5c summarized from Figure S6 and S7. It was presented that bubble sizes became larger as the  $\text{CO}_2$  injecting. Due to the impact of gas density and buoyancy force, the heavier gas preferred to have a relatively larger bubble size in the same solution [52–54]. Hence, the generated bubble sizes of  $\text{H}_2$  are generally smaller than the one of CO under the same locations and conditions, which provided a

basis for the identification of products [53]. Combined with the results that the selectivity to CO approaching 100% at the potential of  $-0.65$  V in Fig. 2c, it was further indicated that all reaction regions in Fig. 5b are afforded to CO generation and the injection of  $\text{CO}_2$  could suppress the occurrence of HER. The same phenomenon can be observed at the electrolysis potential of  $-0.7$  V. In Figs. 5d and 6 reaction regions for HER were observed in an Ar-saturated electrolyte, while additional 10 regions in the  $\text{CO}_2$ -saturated electrolyte as shown in Fig. 5e. Summarizing from Figs. S8 and S9, Fig. 5f showed that bubble size increased when the gas atmosphere changing Ar to  $\text{CO}_2$ , meaning that the product gas transferred from

H<sub>2</sub> to CO. On the other hand, only one newly emerged reaction region for CO<sub>2</sub>RR was presented in Fig. 5e, while there were 3 ones for the HER in Fig. 5d. This difference indicated that the reaction regions for CO<sub>2</sub>RR could almost fully activate the region of insufficient conditioning for the HER at the same potential. The visualization results unveiled that the applied potential has a great impact on the number of reaction regions. When the cathodic potential increased from −0.65 V to −0.7 V, the number of reaction regions increased from 12 to 16 under the CO<sub>2</sub> environment. Combining the results from Figs. 3 and 4, the high cathodic potential increases not only the product yield rate of CO per single reaction regions, but also the number of reaction regions.

Supplementary data related to this article can be found at <https://doi.org/10.1016/j.mtphys.2021.100427>.

#### 4. Conclusion

In summary, the molecular dispersion catalyst of NiPc-OMe shows outstanding ability towards CO formation with Faradic efficiency (FE) above 98% over a wide potential range from −0.55 V to −0.77 V vs. RHE due to the well-defined Ni–N<sub>4</sub> catalytically active sites. Combining the high-speed and micro-scale visualization technique with the electrochemical test system provides a directly optical view of the continued CO generation on the electrode in the CO<sub>2</sub>-saturated 0.5 M KHCO<sub>3</sub> electrolyte. By the visualized comparisons of bubble generation under CO<sub>2</sub> and Ar saturated electrolytes, the highly selective catalytic ability of NiPc-OMe for CO<sub>2</sub>RR are verified. Additionally, CO bubble behaviors can be influenced by the applied cathodic potential. The increased overpotential not only enhances the gas production rate of single reaction region, but also increases the number of reaction regions. This study provides a novel characterization method for the CO<sub>2</sub> electrolyzer using high-speed camera for advancing the research of electrocatalysts for CO<sub>2</sub>RR. This novel method also provides better understanding for electrode design of the CO<sub>2</sub> electrolyzer to speed up the process from the lab-scale investigation into industrial application.

#### Data availability

Data can be made available on request to the corresponding authors.

#### Declaration of competing interest

The authors declare that they have no known competing financial interests or personal relationships that could have appeared to influence the work reported in this paper.

#### Acknowledgments

The authors greatly appreciate the support from U.S. Department of Energy's Office of Energy Efficiency and Renewable Energy (EERE) under the Fuel Cell Technologies Office Award Number DE-EE0008426 and DE-EE0008423, and National Energy Technology Laboratory under Award DE-FE0011585. Y.Y. acknowledges the funding support from the Advanced Manufacturing Institute of University of Houston. A portion of the research used resources of the Advanced Photon Source (12-BM), a U.S. Department of Energy (DOE) Office of Science User Facility operated for the DOE Office of Science by Argonne National Laboratory under Contract No. DE-AC02-06CH11357. The authors also wish to express their appreciation to Alexander Terekhov, Douglas Warnberg, and Dr. Brian Canfield for their help.

#### Appendix A. Supplementary data

Supplementary data to this article can be found online at <https://doi.org/10.1016/j.mtphys.2021.100427>.

#### Credit author statement

Kui Li: Conceptualization, Methodology, Data curation (Visualization observation via high-speed and micro-scale visualization system), Writing – original draft, Investigation, Validation, Writing – review & editing. Weitian Wang: Conceptualization, Data curation, Investigation, Validation, Writing – review & editing. Hongzhi Zheng: Methodology, Data curation (Electrochemical test of electrochemical CO<sub>2</sub> reduction and product detection and analysis), Writing – original draft, Investigation, Validation, Writing – review & editing. Xiaojun Wang: Methodology, Validation, Writing – review & editing. Zhiqiang Xie: Methodology, Validation, Writing – review & editing. Lei Ding: Writing – review & editing. Shule Yu: Writing – review & editing. Yan Yao: Conceptualization, Methodology, Supervision, Validation, Writing – review & editing. Feng-Yuan Zhang: Conceptualization, Methodology, Supervision, Validation, Writing – review & editing.

#### References

- [1] M. Liu, Y.J. Pang, B. Zhang, P. De Luna, O. Voznyy, J.X. Xu, X.L. Zheng, C.T. Dinh, F.J. Fan, C.H. Cao, F.P.G. de Arquer, T.S. Safaei, A. Mepham, A. Klinkova, E. Kumacheva, T. Filleter, D. Sinton, S.O. Kelley, E.H. Sargent, Enhanced electrocatalytic CO<sub>2</sub> reduction via field-induced reagent concentration, *Nature* 537 (2016) 382–386.
- [2] M. Zhong, K. Tran, Y.M. Min, C.H. Wang, Z.Y. Wang, C.T. Dinh, P. De Luna, Z.Q. Yu, A.S. Rasouli, P. Brodersen, S. Sun, O. Voznyy, C.S. Tan, M. Askerka, F.L. Che, M. Liu, A. Seifitokaldani, Y.J. Pang, S.C. Lo, A. Ip, Z. Ulissi, E.H. Sargent, Accelerated discovery of CO<sub>2</sub> electrocatalysts using active machine learning, *Nature* 581 (2020) 178–183.
- [3] Z. Wang, J. Fan, B. Cheng, J. Yu, J. Xu, Nickel-based cocatalysts for photocatalysis: hydrogen evolution, overall water splitting and CO<sub>2</sub> reduction, *Mater. Today Phys.* 15 (2020) 100279.
- [4] R. Cheng, C.C. Chung, S. Wang, B. Cao, M. Zhang, C. Chen, Z. Wang, M. Chen, S. Shen, S.P. Feng, Three-dimensional self-attaching perovskite quantum dots/polymer platform for efficient solar-driven CO<sub>2</sub> reduction, *Mater. Today Phys.* 17 (2021) 100358.
- [5] J.K. Mo, Z.Y. Kang, S.T. Retterer, D.A. Cullen, T.J. Toops, J.B. Green, M.M. Mench, F.Y. Zhang, Discovery of true electrochemical reactions for ultrahigh catalyst mass activity in water splitting, *Sci. Adv.* 2 (2016): e160069.
- [6] G. Yang, S. Yu, Z. Kang, Y. Li, G. Bender, B.S. Pivovar, J.B. Green Jr., D.A. Cullen, F.Y. Zhang, Building electron/proton nanohighways for full utilization of water splitting catalysts, *Adv Energy Mater* 10 (2020) 1903871.
- [7] K. Li, Y. Li, Y. Wang, J. Ge, C. Liu, W. Xing, Enhanced electrocatalytic performance for the hydrogen evolution reaction through surface enrichment of platinum nanoclusters alloying with ruthenium in situ embedded in carbon, *Environ. Eng. Sci.* 11 (2018) 1232–1239.
- [8] Z. Kang, G. Yang, J. Mo, Y. Li, S. Yu, D.A. Cullen, S.T. Retterer, T.J. Toops, G. Bender, B.S. Pivovar, J.B. Green, F.-Y. Zhang, Novel thin/tunable gas diffusion electrodes with ultra-low catalyst loading for hydrogen evolution reactions in proton exchange membrane electrolyzer cells, *Nanomater. Energy* 47 (2018) 434–441.
- [9] Z.Y. Kang, J.K. Mo, G.Q. Yang, S.T. Retterer, D.A. Cullen, T.J. Toops, J.B. Green, M.M. Mench, F.Y. Zhang, Investigation of thin/well-tunable liquid/gas diffusion layers exhibiting superior multifunctional performance in low-temperature electrolytic water splitting, *Environ. Eng. Sci.* 10 (2017) 166–175.
- [10] J.K. Mo, Z.Y. Kang, G.Q. Yang, Y.F. Li, S.T. Retterer, D.A. Cullen, T.J. Toops, G. Bender, B.S. Pivovar, J.B. Green, F.Y. Zhang, In situ investigation on ultrafast oxygen evolution reactions of water splitting in proton exchange membrane electrolyzer cells, *J. Mater. Chem.* 5 (2017) 18469–18475.
- [11] B. Pivovar, N. Rustagi, S. Satyapal, Hydrogen at scale (H<sub>2</sub>@Scale) key to a clean, economic, and sustainable energy system, *Electrochem Soc Interface* 27 (2018) 47–52.
- [12] C. Hepburn, E. Adlen, J. Beddington, E.A. Carter, S. Fuss, N. Mac Dowell, J.C. Minx, P. Smith, C.K. Williams, The technological and economic prospects for CO<sub>2</sub> utilization and removal, *Nature* 575 (2019) 87–97.
- [13] C.J. Chen, X.F. Sun, X.P. Yan, Y.H. Wu, H.Z. Liu, Q.G. Zhu, B.B.A. Bediako, B.X. Han, Boosting CO<sub>2</sub> electroreduction on N,P-Co-doped carbon aerogels, *Angew. Chem. Int. Ed.* 59 (2020) 11123–11129.
- [14] K. Jiang, R.B. Sandberg, A.J. Akey, X. Liu, D.C. Bell, J.K. Nørskov, K. Chan, H. Wang, Metal ion cycling of Cu foil for selective C–C coupling in electrochemical CO<sub>2</sub> reduction, *Nat. Catal* 1 (2018) 111–119.

- [15] H.B. Yang, S.-F. Hung, S. Liu, K. Yuan, S. Miao, L. Zhang, X. Huang, H.-Y. Wang, W. Cai, R. Chen, J. Gao, X. Yang, W. Chen, Y. Huang, H.M. Chen, C.M. Li, T. Zhang, B. Liu, Atomically dispersed Ni(i) as the active site for electrochemical CO<sub>2</sub> reduction, *Nat. Energy* 3 (2018) 140–147.
- [16] N. Han, Y. Wang, H. Yang, J. Deng, J.H. Wu, Y.F. Li, Y.G. Li, Ultrathin bismuth nanosheets from in situ topotactic transformation for selective electrocatalytic CO<sub>2</sub> reduction to formate, *Nat. Commun.* 9 (2018) 1–8.
- [17] B. Jiang, X.G. Zhang, K. Jiang, D.Y. Wu, W.B. Cai, Boosting formate production in electrocatalytic CO<sub>2</sub> reduction over wide potential window on Pd surfaces, *J. Am. Chem. Soc.* 140 (2018) 2880–2889.
- [18] X.L. Zheng, P. De Luna, F.P.G. de Arquer, B. Zhang, N. Becknell, M.B. Ross, Y.F. Li, M.N. Banis, Y.Z. Li, M. Liu, O. Voznyy, C.T. Dinh, T.T. Zhuang, P. Stadler, Y. Cui, X.W. Du, P.D. Yang, E.H. Sargent, Sulfur-modulated tin sites enable highly selective electrochemical reduction of CO<sub>2</sub> to formate, *Joule* 1 (2017) 794–805.
- [19] Y. Wu, Z. Jiang, X. Lu, Y. Liang, H. Wang, Domino electroreduction of CO<sub>2</sub> to methanol on a molecular catalyst, *Nature* 575 (2019) 639–642.
- [20] X. Zhang, Y. Wang, M. Gu, M. Wang, Z. Zhang, W. Pan, Z. Jiang, H. Zheng, M. Lucero, H. Wang, G.E. Sterbinsky, Q. Ma, Y.-G. Wang, Z. Feng, J. Li, H. Dai, Y. Liang, Molecular engineering of dispersed nickel phthalocyanines on carbon nanotubes for selective CO<sub>2</sub> reduction, *Nat. Energy* 5 (2020) 684–692.
- [21] J. Chen, Z. Wang, H. Lee, J. Mao, C.A. Grimes, C. Liu, M. Zhang, Z. Lu, Y. Chen, S.P. Feng, Efficient electroreduction of CO<sub>2</sub> to CO by Ag-decorated S-doped g-C<sub>3</sub>N<sub>4</sub>/CNT nanocomposites at industrial scale current density, *Mater. Today Phys.* 12 (2020) 100176.
- [22] S. Gao, Y. Lin, X. Jiao, Y. Sun, Q. Luo, W. Zhang, D. Li, J. Yang, Y. Xie, Partially oxidized atomic cobalt layers for carbon dioxide electroreduction to liquid fuel, *Nature* 529 (2016) 68–71.
- [23] Y. Wang, Z. Chen, P. Han, Y. Du, Z. Gu, X. Xu, G. Zheng, Single-atomic Cu with multiple oxygen vacancies on ceria for electrocatalytic CO<sub>2</sub> reduction to CH<sub>4</sub>, *ACS Catal.* 8 (2018) 7113–7119.
- [24] A. Gallo, J.L. Snider, D. Sokaras, D. Nordlund, T. Kroll, H. Ogasawara, L. Kovarik, M.S. Duyar, T.F. Jaramillo, Ni<sub>5</sub>Ga<sub>3</sub> catalysts for CO<sub>2</sub> reduction to methanol: exploring the role of Ga surface oxidation/reduction on catalytic activity, *Appl. Catal., B* 267 (2020) 118369.
- [25] C.-T. Dinh, T. Burdyny, M.G. Kibria, A. Seifitokaldani, C.M. Gabardo, F.P. García De Arquer, A. Kiani, J.P. Edwards, P. De Luna, O.S. Bushuyev, C. Zou, R. Quintero-Bermudez, Y. Pang, D. Sinton, E.H. Sargent, CO<sub>2</sub> electroreduction to ethylene via hydroxide-mediated copper catalysis at an abrupt interface, *Science* 360 (2018) 783–787.
- [26] F.P. García De Arquer, C.-T. Dinh, A. Ozden, J. Wicks, C. McCallum, A.R. Kirmani, D.-H. Nam, C. Gabardo, A. Seifitokaldani, X. Wang, Y.C. Li, F. Li, J. Edwards, L.J. Richter, S.J. Thorpe, D. Sinton, E.H. Sargent, CO<sub>2</sub> electrolysis to multicarbon products at activities greater than 1 A cm<sup>-2</sup>, *Science* 367 (2020) 661–666.
- [27] T.-T. Zhuang, Z.-Q. Liang, A. Seifitokaldani, Y. Li, P. De Luna, T. Burdyny, F. Che, F. Meng, Y. Min, R. Quintero-Bermudez, C.T. Dinh, Y. Pang, M. Zhong, B. Zhang, J. Li, P.-N. Chen, X.-L. Zheng, H. Liang, W.-N. Ge, B.-J. Ye, D. Sinton, S.-H. Yu, E.H. Sargent, Steering post-C–C coupling selectivity enables high efficiency electroreduction of carbon dioxide to multi-carbon alcohols, *Nat. Catal.* 1 (2018) 421–428.
- [28] D. Ren, N.T. Wong, A.D. Handoko, Y. Huang, B.S. Yeo, Mechanistic insights into the enhanced activity and stability of agglomerated Cu nanocrystals for the electrochemical reduction of carbon dioxide to propanol, *J. Phys. Chem. Lett.* 7 (2016) 20–24.
- [29] S. Verma, B. Kim, H.-R.M. Jhong, S. Ma, P.J.A. Kenis, A gross-margin model for defining techno-economic benchmarks in the electroreduction of CO<sub>2</sub>, *ChemSuschem* 9 (2016) 1972–1979.
- [30] K.P. Kuhl, E.R. Cave, D.N. Abram, T.F. Jaramillo, New insights into the electrochemical reduction of carbon dioxide on metallic copper surfaces, *Environ. Eng. Sci.* 5 (2012) 7050–7059.
- [31] Y. Zhong, S. Wang, M. Li, J. Ma, S. Song, A. Kumar, H. Duan, Y. Kuang, X. Sun, Rational design of copper-based electrocatalysts and electrochemical systems for CO<sub>2</sub> reduction: from active sites engineering to mass transfer dynamics, *Mater. Today Phys.* 18 (2021) 100354.
- [32] L. Wang, L. Wang, Y. Du, X. Xu, S.X. Dou, Progress and perspectives of bismuth oxyhalides in catalytic applications, *Mater. Today Phys.* 16 (2021) 100294.
- [33] S. Nitopi, E. Bertheussen, S.B. Scott, X. Liu, A.K. Engstfeld, S. Horch, B. Seger, I.E.L. Stephens, K. Chan, C. Hahn, J.K. Nørskov, T.F. Jaramillo, I. Chorkendorff, Progress and perspectives of electrochemical CO<sub>2</sub> reduction on copper in aqueous electrolyte, *Chem. Rev.* 119 (2019) 7610–7672.
- [34] Y. Hori, H. Wakebe, T. Tsukamoto, O. Koga, Electrocatalytic process of CO selectivity in electrochemical reduction of CO<sub>2</sub> at metal electrodes in aqueous media, *Electrochim. Acta* 39 (1994) 1833–1839.
- [35] Y. Hori, R. Takahashi, Y. Yoshinami, A. Murata, Electrochemical reduction of CO at a copper electrode, *J. Phys. Chem. B* 101 (1997) 7075–7081.
- [36] Y. Hori, K. Kikuchi, A. Murata, S. Suzuki, Production of methane and ethylene in electrochemical reduction of carbon dioxide at copper electrode in aqueous hydrogencarbonate solution, *Chem. Lett.* 15 (1986) 897–898.
- [37] R. Kortlever, J. Shen, K.J.P. Schouten, F. Calle-Vallejo, M.T.M. Koper, Catalysts and reaction pathways for the electrochemical reduction of carbon dioxide, *J. Phys. Chem. Lett.* 6 (2015) 4073–4082.
- [38] H.A. Hansen, J.B. Varley, A.A. Peterson, J.K. Nørskov, Understanding trends in the electrocatalytic activity of metals and enzymes for CO<sub>2</sub> reduction to CO, *J. Phys. Chem. Lett.* 4 (2013) 388–392.
- [39] A.H. Reed, E. Yeager, Infra-red internal reflexion studies of the germanium/electrolyte interface, *Electrochim. Acta* 15 (1970) 1345–1354.
- [40] A. Bewick, K. Kunimatsu, Infra red spectroscopy of the electrode–electrolyte interphase, *Surf. Sci.* 101 (1980) 131–138.
- [41] M. Osawa, M. Ikeda, Surface-enhanced infrared absorption of p-nitrobenzoic acid deposited on silver island films: contributions of electromagnetic and chemical mechanisms, *J. Phys. Chem.* 95 (1991) 9914–9919.
- [42] B. Jiang, X.-G. Zhang, K. Jiang, D.-Y. Wu, W.-B. Cai, Boosting formate production in electrocatalytic CO<sub>2</sub> reduction over wide potential window on Pd surfaces, *J. Am. Chem. Soc.* 140 (2018) 2880–2889.
- [43] W. Deng, L. Zhang, L. Li, S. Chen, C. Hu, Z.-J. Zhao, T. Wang, J. Gong, Crucial role of surface hydroxyls on the activity and stability in electrochemical CO<sub>2</sub> reduction, *J. Am. Chem. Soc.* 141 (2019) 2911–2915.
- [44] M.F. Baruch, J.E. Pander, J.L. White, A.B. Bocarsly, Mechanistic insights into the reduction of CO<sub>2</sub> on tin electrodes using in situ ATR-IR spectroscopy, *ACS Catal.* 5 (2015) 3148–3156.
- [45] S.-J. Kim, M. Matsumoto, K. Shigehara, Synthesis and electrical properties of poly(μ-1,4-diisocyanobenzene) octacyanophthalocyaninatoiron(II), *Synthetic Met* 107 (1999) 27–33.
- [46] E.I. Yslas, V. Rivarola, E.N. Durantini, Synthesis and photodynamic activity of zinc(II) phthalocyanine derivatives bearing methoxy and trifluoromethylbenzyloxy substituents in homogeneous and biological media, *Bioorg. Med. Chem.* 13 (2005) 39–46.
- [47] Y. Li, Z. Kang, X. Deng, G. Yang, S. Yu, J. Mo, D.A. Talley, G.K. Jennings, F.-Y. Zhang, Wettability effects of thin titanium liquid/gas diffusion layers in proton exchange membrane electrolyzer cells, *Electrochim. Acta* 298 (2019) 704–708.
- [48] L.A. Avakyan, A.S. Manukyan, A.A. Mirzakhanyan, E.G. Sharoyan, Y.V. Zubavichus, A.L. Trigub, N.A. Kolpacheva, L.A. Bugaev, Atomic structure of nickel phthalocyanine probed by X-ray absorption spectroscopy and density functional simulations, *Opt Spectrosc.* 114 (2013) 347–352.
- [49] D.-D. Ma, S.-G. Han, C. Cao, X. Li, X.-T. Wu, Q.-L. Zhu, Remarkable electrocatalytic CO<sub>2</sub> reduction with ultrahigh CO/H<sub>2</sub> ratio over single-molecularly immobilized pyrrolidinonyl nickel phthalocyanine, *Appl. Catal., B* 264 (2020) 118530.
- [50] D.-D. Ma, S.-G. Han, C. Cao, W. Wei, X. Li, B. Chen, X.-T. Wu, Q.-L. Zhu, Bifunctional single-molecular heterojunction enables completely selective CO<sub>2</sub>-to-CO conversion integrated with oxidative 3D nano-polymerization, *Environ. Eng. Sci.* 14 (2021) 1544–1552.
- [51] S. Liu, H.B. Yang, S.F. Hung, J. Ding, W. Cai, L. Liu, J. Gao, X. Li, X. Ren, Z. Kuang, Y. Huang, T. Zhang, B. Liu, Elucidating the electrocatalytic CO<sub>2</sub> reduction reaction over a model single-atom nickel catalyst, *Angew. Chem. Int. Ed.* 59 (2020) 798–803.
- [52] Y.F. Li, G.Q. Yang, S.L. Yu, Z.Y. Kang, J.K. Mo, B. Han, D.A. Talley, F.Y. Zhang, In-situ investigation and modeling of electrochemical reactions with simultaneous oxygen and hydrogen microbubble evolutions in water electrolysis, *Int. J. Hydrogen Energy* 44 (2019) 28283–28293.
- [53] K. Matsuura, Y. Yamanishi, C. Guan, S. Yanase, Control of hydrogen bubble plume during electrolysis of water, *J. Phys. Commun.* 3 (2019): 035012.
- [54] Y. Li, G. Yang, S. Yu, J. Mo, K. Li, Z. Xie, L. Ding, W. Wang, F.-Y. Zhang, High-speed characterization of two-phase flow and bubble dynamics in titanium felt porous media for hydrogen production, *Electrochim. Acta* 370 (2021) 137751.